Activation of a Ni electrocatalyst through spontaneous transformation of nickel sulfide to nickel hydroxide in an oxygen evolution reaction

Minoh Lee[a], Hyung-Suk Oh[a], Min Kyung Cho[b], Jae-Pyoung Ahn[b], Yun Jeong Hwang[a,c,*], Byoung Koun Min[a,d,*]

[a] Clean Energy Research Center, Korea Institute of Science and Technology, Seoul 02792, Republic of Korea
[b] Advanced Analysis Center, Korea Institute of Science and Technology, Seoul 02792, Republic of Korea
[c] Division of Energy and Environmental Technology, KIST School, Korea University of Science and Technology (UST), Seoul 02792, Republic of Korea
[d] Green School, Korea University, Seoul 02841, Republic of Korea

ABSTRACT

Ni-sulfide compounds synthesized on Ni foam by simple thermal sulfurization are employed as electrocatalysts for water oxidation, resulting in superior activity in alkaline electrolyte media. The role of sulfur in Ni-sulfide was found to be an activator that transformed sulfide into hydroxide, which was eventually transformed into (oxy)hydroxide. The Ni-(oxy)hydroxide phase was also found to be layered and/or amorphous. This activated catalyst showed significant enhancement in water oxidation performance with a low overpotential value of 256 mV at current density of 10 mA cm^{-2}. Our observation could offer important insight into metal-chalcogenide electrocatalyst for water oxidation.

1. Introduction

Electrochemical water splitting is considered to be an attractive and efficient method to produce pure hydrogen in connection with renewable energy [1]. In general, the overall water splitting process can be divided into two half-cell redox reactions: a hydrogen evolution reaction (HER) and an oxygen evolution reaction (OER) [2]. In particular, a high overpotential is required for OER due to the sluggish kinetics associated with O−H bond breaking and attendant O−O bond formation. Therefore, the OER has been regarded as a bottle-neck in commercializing a water splitting system [3,4]. Hence, an efficient OER electrocatalyst is highly desired to address this challenge by efficiently coupling multiple protons and electron transfers for O$_2$ evolution at low overpotential [5]. Currently, RuO$_2$, IrO$_2$, and their mixed oxide (e.g., Ru$_{1-x}$Ir$_x$O$_2$) are regarded as the most efficient OER electrocatalysts [6–8]. However, these noble metal-based catalysts have obvious disadvantages for practical applications due to their low earth abundance and high cost.

To overcome this issue, several studies have developed non-noble metal based OER electrocatalysts, including low-cost transition metal oxide/hydroxides [9–13], perovskite, [14–16] chalcogenides, [17–19] phosphates [20], and molecular electrocatalysts [21–23]. Among these metal-chalcogenide OER electrocatalysts such as MX, MX$_2$, M$_9$X$_8$, M$_3$X$_4$, and M$_3$X$_2$ (M = Co and Ni, X = S, Se, and Te) have recently received

attention as strong alternatives due to their prominent electronic structure and low cost [24–27].

Ni-sulfides compounds (Ni$_3$S$_2$, NiS, NiS$_2$ etc) have recently shown huge potential as efficient OER electrocatalysts [27–32]. In the case of Ni$_3$S$_2$ metal-chalcogenide, Ni$_3$S$_2$ nanorods/Ni foam composite electrode has been demonstrated as an excellent OER catalyst with a low overpotential of 157 mV [17]. The high activity of this catalyst was explained in terms of unusual Ni mixed valance states (Ni°, Ni$^+$, and Ni^{2+}) due to synergetic chemical coupling effects among hydrated Ni$_3$S$_2$ nanorods, the nickel oxide layer, and the Ni foam support. On the other hand, the role of sulfur in the high activity has also been studied in Ni-sulfide. For example, when Ni$_x$S$_y$ film is synthesized by pulse-electrodeposition, it has been proposed that sulfur anion is depleted in the electrocatalyst surface layer while Ni$_x$S$_y$ is converted into an amorphous Ni oxide [29]. This implies that metal sulfide can act as a precursor to a highly active Ni oxide electrocatalyst for oxygen evolution. Despite several important insights from previous studies, the origin of the enhanced performance of Ni$_3$S$_2$/Ni electrocatalyst has not been clearly understood yet. The physical origin of the experimentally-observed enhanced performance of activated Ni$_x$S$_y$ OER electrocatalyst in alkaline condition has not been elucidated either. Therefore, a more detailed study is needed to advance metal-chalcogenide electrocatalysts for OER.

The objective of this report was to address these issues mentioned

* Corresponding authors at: Clean Energy Research Center, Korea Institute of Science and Technology, Seoul 02792, Republic of Korea.
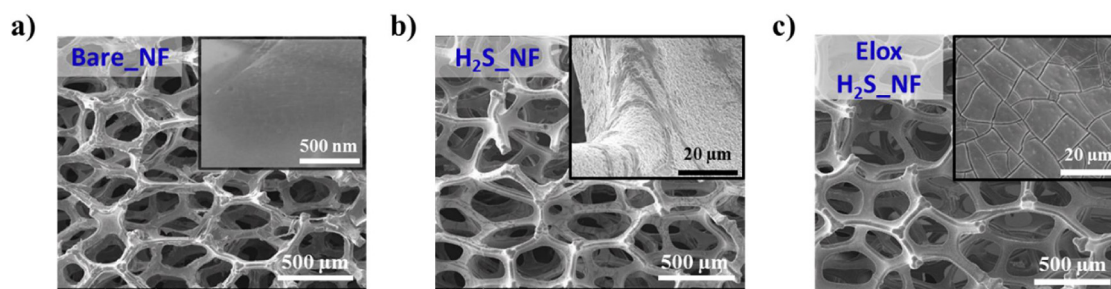 *E-mail addresses:* yjhwang@kist.re.kr (Y.J. Hwang), bkmin@kist.re.kr (B.K. Min).

Fig. 1. SEM images of bare Ni foam and sulfurized Ni foam before and after electrochemical activation: (a) Bare Ni foam (Bare_NF), (b) As-prepared sulfurized Ni foam (H₂S_NF), (c) Electrochemically activated sulfurized Ni foam (Elox_H₂S_NF).

above and suggest a role of sulfur in Ni_xS_y OER electrocatalyst. A simple method to synthesize active OER catalyst via a two-step spontaneous transformation (from sulfide to hydroxide ($Ni(OH)_2$) and from (Ni $(OH)_2$) to γ-NiOOH in alkaline condition) was described in this study. The γ-NiOOH phase was found to be amorphous and/or layered, providing a great number of defect sites. It might also be used as incorporation site for Fe-impurity in KOH electrolyte. Such observation provides significant insights to metal-chalcogenide electrocatalysts for OER.

2. Experimental

2.1. Preparation of the anode electrode

A Ni foam (NF) was purchased from MTI Corp.. It was cut into $1 \times 2 \, cm^2$ and cleaned via sonication in ethanol and deionized water. The NF was then dried and moved into a tube furnace. Hydrogen disulfide gas (1% H_2S with Nitrogen carrier gas) treatment was subsequently carried out at 300 ℃ for 1 h followed by cooling down to room temperature. The prepared Ni-sulfide (H₂S_NF) was then used as a working electrode for water oxidation.

2.2. Electrochemical measurements

All electrochemical measurements were performed using a potentiostat (Ivium, Iviumtechnology) with a three-compartment electrochemical cell. The prepared NF was used as a working electrode. It was exposed into the electrolyte with an active area of $1 \, cm^2$. A platinum wire was used as counter. The reference electrode of Hg/HgO was used in 1.0 M KOH solution. Ag/AgCl was used in CO_2-saturated bicarbonate electrolyte. Electrochemical oxidation treatment was performed using cyclic voltammetry from 0.9 to 1.6 V_{RHE} for 10 cycles. For neutral electrolyte experiments, 0.5 M $KHCO_3$ (99.7%, Sigma-Aldrich) electrolyte (pH 7.3) was prepared in Millipore water (resistivity $> 18 \, M\Omega cm$). CO_2 (99.999%, Shinyang Sanso Co.) gas was saturated in the electrolyte and continuously injected during measurements. Reference electrodes were calibrated to RHE using the following two equations, (1) E (vs. RHE) = E (vs. Hg/HgO) + 0.11 + 0.059 V × pH, and (2) E (vs. RHE) = E (vs. Ag/AgCl) + 0.21 + 0.059 V × pH. Ohmic loss was calculated from EIS results. Frequency range varied from 10 kHz down to 10 mHz with a signal amplitude of 10 mV rms. To measure the concentration of gaseous products (e.g., H_2 and O_2), the closed electrochemical cell was connected with a gas chromatography (Younglin 6500 GC) equipped with a capillary column (Restek, RT®-Msieve 5 A) and pulsed discharge detector (PDD). He (99.999%, Shinyang Sanso Co.) was employed as a carrier gas.

2.3. Characterization

X-ray diffractometer (XRD, Shimadzu, XRD-6000) measurements were conducted using Cu $K\alpha$ radiation (0.15406 nm). A scanning electron microscope (SEM, FEI, Nova-Nano200) at 10 kV acceleration voltage was employed to investigate surface morphologies of the prepared samples. X-ray photoelectron spectroscopy (XPS) measurements were carried out on a PHI 5000 VersaProbe (Ulvan-PHI) equipped with monochromatic X-rays generated by an Al Ka (1486.6 eV) source. Raman spectroscopy (Alpha 300 S, WITec) equipped with an Nd:Yag laser (excitation wavelength of 532 nm) was employed to investigate structures of these samples. Three-dimensional depth profiling was carried out using time-of-flight secondary ion mass spectrometry (TOF-SIMS) where 10-keV Cs + beam was employed. A transmission electron microscopy analysis including diffraction pattern was performed using a FEI TitanTM 80–300 microscope operating at 300 kV. For elemental mapping analysis, Super-X EDS was employed using FEI Talos F200X at 200 kV.

3. Results and discussion

3.1. Sulfurization and electro-oxidation of Ni foam

Sulfurized Ni was synthesized by direct treatment of H_2S-containing gas (1% H_2S/N_2) on Ni foam (denoted as H₂S_NF). Ni foam was used as a Ni source and a substrate of H₂S_NF electrocatalyst because metal foam has zig-zag skeleton and their high porosity could increase active surface area [13,33–35]. The as-synthesized H₂S_NF was electrochemically oxidized with 10 cycles of cyclic voltammetric potential sweeps ranging from + 0.9 to +1.6 V_{RHE} (denoted as Elox_H₂S_NF). Its voltammogram is shown in Fig. S1 (Supporting Information). This electrochemical oxidation process resulted in the formation of oxidized Ni electrocatalyst prior to electrochemical water oxidation.

To understand morphology changes during sulfurization and electro-oxidation process, scanning electron microscopy (SEM) images were taken (Fig. 1). For comparison, bare Ni foam (denoted as Bare_NF) was also measured. Unlike Bare_NF (Fig. 1a), the surface of H₂S_NF was slightly roughen after sulfurization (Fig. 1b). Magnified image (inset in Fig. 1b) revealed slightly wrinkled surface with irregular crack formation. A more detailed morphology of H₂S_NF is shown in Fig. S2 (Supporting Information). Its crack trace size was around 1 μm. The volume expansion induced by a new Ni crystal phase transition during sulfurization might cause unexpected crack formation. For Elox_H₂S_NF, its crack trace size was expanded up to 20 μm plausibly due to more severe swelling or volume expansion during electrochemical oxidation treatment as shown in Fig. S2b (Supporting Information) [36]. This result was interpreted in terms of transformation of Ni-sulfide into oxidized Ni. This will be discussed below with more detailed material characterizations.

The structure of the electrochemically oxidized Ni-sulfide (Elox_H₂S_NF) was further characterized using transmission electron microscopy (TEM) as shown in Fig. 2. The high-angle annular dark-field imaging (HAADF) of Elox_H₂S_NF (Fig. 2a) showed two different phases against the boundary placed in the center (yellow dashed line). A (left) and B (right) regions are the bulk and surface of Elox_H₂S_NF, respectively. The Ni-sulfide in the A-region showed a nearly uniform contrast,
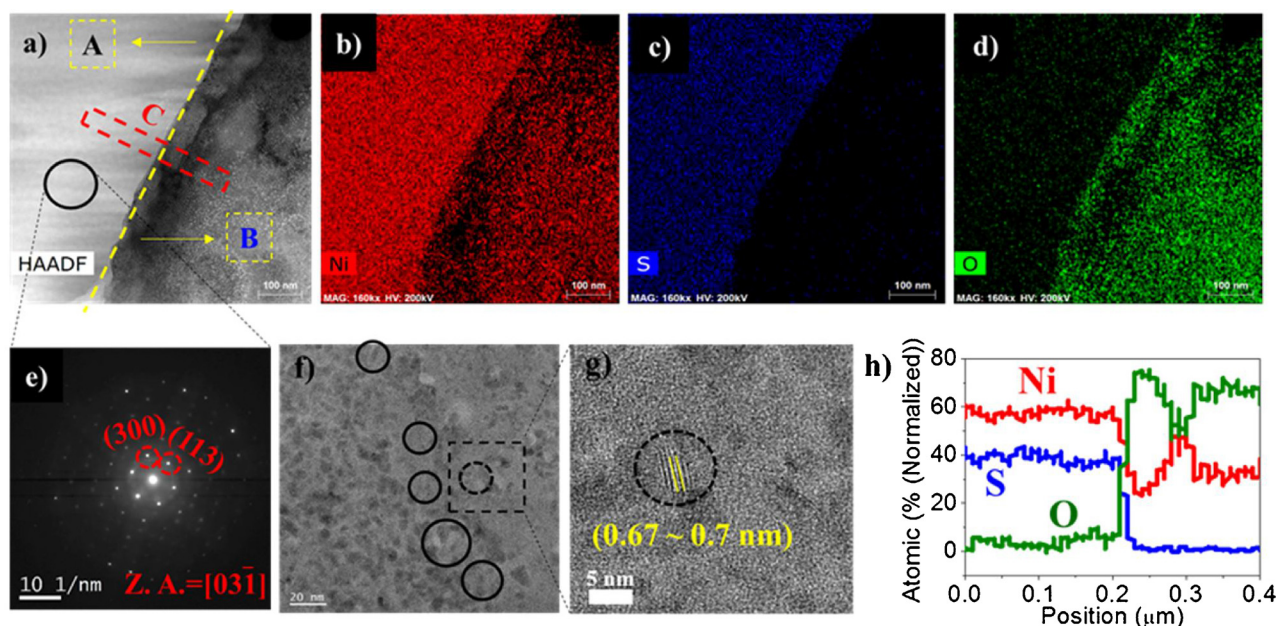
Fig. 2. Cross-section of electrochemically oxidized Ni sulfide (Elox_H₂S_NF). (a) HAADF-STEM image of Elox_H₂S_NF and corresponding EDX elemental maps shown in panel (a); Ni in (b), S in (c) and O in (d). (e) SAED pattern for the area marked with black circle in the STEM image. (f) High-resolution TEM image of the B-region indicated in STEM image. (g) Corresponding magnified TEM image. (h) Line profile of the selected C-region indicated in the STEM image.

suggesting a homogeneous morphology and structure. However, B-region generally showed spots. The clear difference in the two phases provided evidence of significant material transformation after electrochemical treatment. To confirm element distribution, corresponding elemental maps of Ni, S, and O were measured. Results are shown in Fig. 2b–d. Elemental Ni was distributed in both regions while sulfur anion was primarily shown in the A-region. However, there was no observable sulfur in the B-region. Oxygen was more heavily detected in the B-region compared to that in the A-region. In the Pourbaix diagram for sulfur-water, sulfur exists in the form of sulfate ion (SO_4^{2-}) under alkaline condition with high potential range. This anion is highly soluble in water, [37–40] supporting our experimental results. Selected-area electron diffraction (SAED) pattern in the A-region is shown in Fig. 2e. Their indexing is well matched with crystalline Ni₃S₂ phase. [41,42] A high-resolution TEM image corresponding to the B-region composed of partially crystalized sub-5 nm nanoparticles (highlighted by black circles) in the amorphous matrix is shown in Fig. 2f. To characterize dark particles in the B-region, the rectangular dot region was magnified (Fig. 2g). The observed lattice fringes of Ni had spacing of 0.67–0.7 nm, corresponding to γ-NiOOH with intercalation sites of anion and water molecules [43]. Formation of γ-NiOOH is associated with swelling and volume expansion of Ni electrode [44]. This was in good agreement with SEM results of Elox_H₂S_NF. For comparison, electrochemically oxidized Bare_NF (from here on denoted Elox_-Bare_NF) was also analyzed using HAADF. Results are shown in Fig. S3 (Supporting Information). The surface of Elox_Bare_NF included a much thinner oxygen rich layer (~20 nm) compared to Elox_H₂S_NF according to EDS-TEM analysis (Figs. 2 and S3, Supporting Information). This implies that sulfur incorporation stimulated a thick layer of electrochemical Ni oxidation. Based on these results, it was proposed that sulfur in Ni-sulfide could be easily replaced by hydroxyl anion after electrochemical oxidation to be converted into mixtures of Ni hydroxides with an amorphous structure and γ-NiOOH.

3.2. Changes of surface state by electro-oxidation

To further elucidate surface properties of the Ni-sulfide foam before and after electrochemical oxidation, various spectroscopic measurements were carried out (Fig. 3), which confirmed oxygen inclusion on the top layer of Ni-sulfide foam by electrochemical treatment. Grazing incident X-ray diffractometer (GIXRD) measurements (Fig. 3a) revealed that sulfurization of the NF had different peaks compared to the XRD pattern of Bare_NF (Fig. S4, Supporting Information). These newly appeared peaks were well matched with various planes of crystalline Ni₃S₂ (JCPDS 44-1418), [41,42] consistent with SAED results (Fig. 2e). After electrochemical oxidation, broad diffraction peaks were additionally observed near 2θ = 20° with a little intense peak at around 26°, demonstrating phases of Ni(OH)₂ and γ-NiOOH [45–49]. Furthermore, intensities of other peaks related to Ni₃S₂ were relatively decreased after electrochemical oxidation, indicating partial conversion from Ni₃S₂ to a hydroxyl-based form on the surface.

Raman spectroscopy was also employed to characterize structures of samples which showed more dramatic changes on the surface (Fig. 3b). Obvious peaks at 202, 224, 305, 326, and 352 cm⁻¹ in Raman shift could be ascribed to Ni-sulfide, in agreement with previous report [50,51]. Intensities of these Ni-S peaks were significantly weakened after the electrochemical oxidation process. A new strong broad peak appeared at ~560 cm⁻¹, corresponding to the vibrational mode of NiOOH [52,53].

Results of X-ray photoelectron spectroscopy (XPS) of Ni 2p and S 2p are shown in Fig. 3c–d, respectively. Ni 2p spectra had two spin-orbit doublet peaks at 855.5 eV (Ni 2p₃/₂) and 873.0 eV (Ni 2p₁/₂) as shown in Fig. S5 (Supporting Information) [54]. Their corresponding satellite resonances were observed at slightly higher binding energy at 861.1 eV (Ni 2p₃/₂) and 873.7 eV (Ni 2p₁/₂). The main peak at 855.7 eV shifted to a lower binding energy region of around 855.3 eV after electrochemical oxidation, corresponding to the peak of NiOOH [55]. The peak of 852.5 eV might be related to the bonding of Ni and S appeared after sulfurization (Fig. S5, Supporting Information). However, this peak has been found to be weakened after electrochemical oxidation [17,28,29]. This result might be due to NiOOH formation on the surface of Ni₃S₂/NF after electrochemical oxidation. Ni (oxy)hydroxide was demonstrated to have γ-NiOOH structure based on HR-TEM as shown in Fig. 2g.

For S 2p XPS spectra, main peaks appeared at 162 and 163 eV corresponding to sulfur signals of S 2p₁/₂ and S 2p₃/₂, respectively. The complete disappearance of these peaks after electrochemical oxidation indicated the loss of sulfur [28,33,56,57]. XPS spectra of O 1 s before
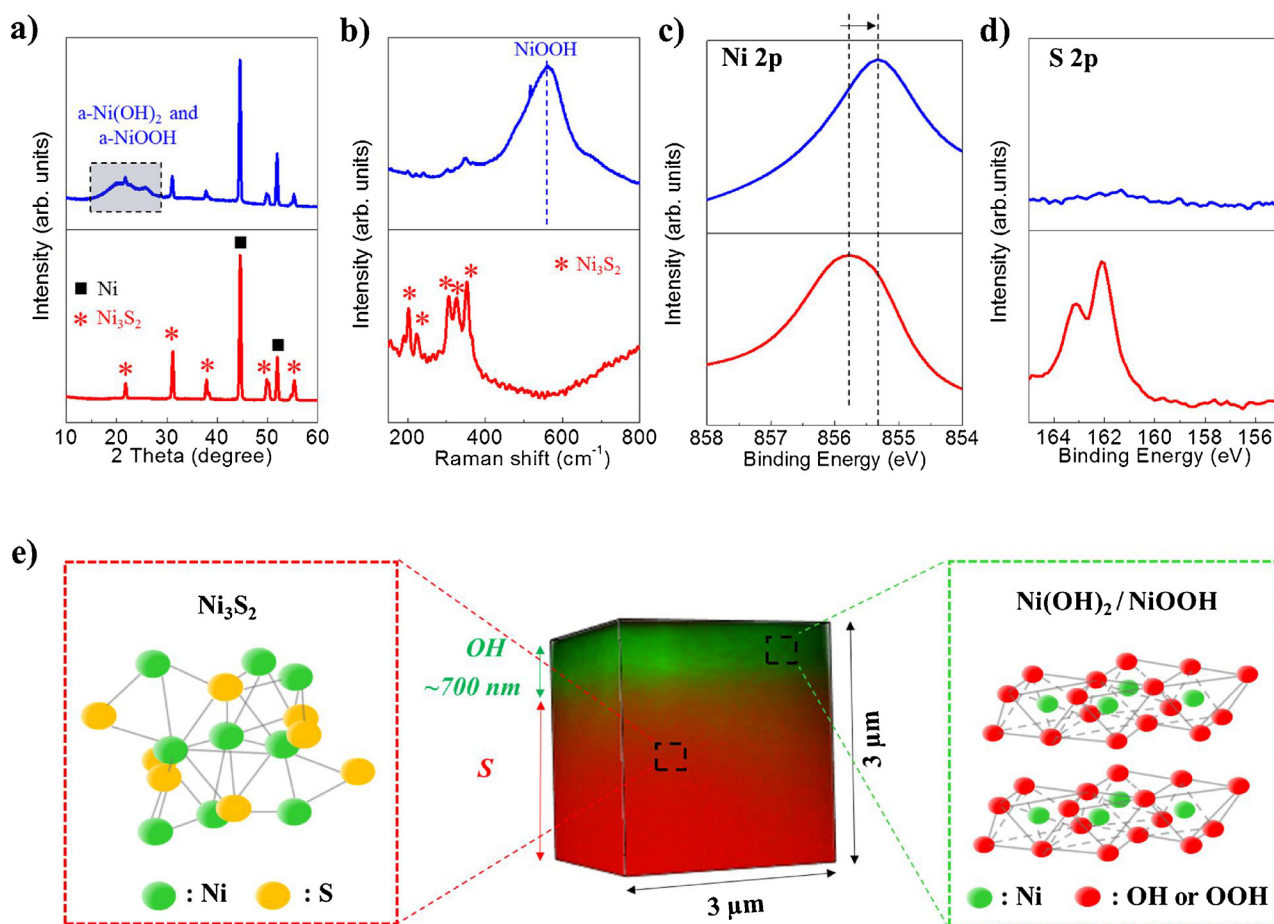
Fig. 3. (a) XRD patterns, (b) Raman spectra, and XPS spectra of (c) Ni 2p and (d) S 2p region of the Ni-sulfide foam (H₂S_NF) before and after electrochemical oxidation. (e) 3D TOF-SIMS image of electrochemically oxidized Ni-sulfide foam (Elox_ H₂S _NF). Different structures of the surface and bulk region in Elox_ H₂S _NF are shown to the left (Ni₃S₂) and right side (Ni(OH)₂ or/and NiOOH), respectively.

and after electrochemical oxidation were also compared (Fig. S6, Supporting Information). Elox_H₂S_NF had a substantially enhanced oxygen peak intensity compared to H₂S_NF. The major peak near 531.1 eV matched with metal-hydroxyl bonding [58]. The peak of adsorbed H₂O molecule was also observed near 533.5 eV. Previous studies have reported that Ni-layered double hydroxide (LDH) by ordered γ-NiOOH can provide intercalation sites for H₂O molecules in their structure [43,59].

Fig. 3e shows a 3-dimensional render of Elox_H₂S_NF from the surface to the bulk region using time-of-flight secondary ion mass spectrometry (TOF-SIMS). In combination with characterization results mentioned earlier, it could be concluded that the primary material in the surface region included Ni hydroxide or Ni (oxy)hydroxide up to 700 nm in thickness while the bulk fraction was composed of Ni₃S₂.

3.3. Water oxidation performance: the role of Ni₃S₂

The catalytic activity of the OER of electrochemically activated Ni-sulfide electrocatalyst (Elox_H₂S_NF) in 1.0 M KOH was examined using cyclic voltammetry (CV). CV curves of Bare_NF, Elox_H₂S_NF, and Elox_Air_NF are shown in Fig. 4a and Fig. S7 (Supporting Information). For comparison, bare NF was also investigated. All samples had anodic peaks between 1.3 and 1.5 V$_{RHE}$ which could be ascribed to Ni(II)/Ni (III) conversion (i.e. Ni(OH)₂ to NiOOH) [11,43,53,60,61]. Bare_NF had the lowest intensity of anodic peak compared to electrochemically oxidized catalysts. This indicates that electrochemical oxidation treatment can facilitate the formation of NiOOH on the nickel foam surface. Elox_H₂S_NF had the highest Ni anodic peak among all samples. As

expected from spectroscopic measurements (Figs. 2,3), the activation of Ni by sulfurization increased Ni oxidation by electrochemical treatment, resulting in an intense anodic peak for Elox_H₂S_NF. In general, the conversion of Ni(OH)₂ to NiOOH occurs via two mechanisms: the solvent mechanism and the proton diffusion mechanism [62,63]. Elox_H₂S_NF with γ-NiOOH structure followed the solvent mechanism in which γ-NiOOH forms through diffusion of OH⁻ as shown in Eq. (1) [62,63].

$$Ni(OH)_2 + OH^- \leftrightarrow NiOOH + H_2O + e^- \tag{1}$$
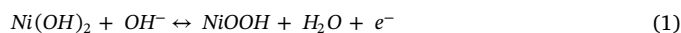
To confirm OER catalytic activity, overpotentials of all catalysts were compared at 10 mA cm^{-2}. The overpotential was chosen as the value of backward scan in the CV curve because it would be a more accurate evaluation compared to forward scan by minimizing the influence of Ni anodic signal. As illustrated in Fig. 4b, Elox_H₂S_NF (256 mV) exhibited a lower overpotential than Bare_NF (361 mV). The overpotential of Elox_H₂S_NF was comparable to that of previously reported Ni-based OER catalyst (Table S1, Supporting Information). The overpotential at a higher current density (100 mA cm^{-2}) was also evaluated. Results showed an identical tendency of overpotential at 10 mA cm^{-2} (Fig. S8, Supporting Information). Elox_H₂S_NF electrocatalyst significantly out-performed all other Ni reference catalysts. The OER catalytic activity was in the following order: Bare_NF < Elox_Air_NF < Elox_Bare_NF < Elox_H₂S_NF. Hence, the enhanced OER activity of electrochemically oxidized Ni-sulfide over non-sulfurized electrocatalysts was attributed to their Ni hydroxide formation, thereby leading to the conversion of Ni(OH)₂ to γ-NiOOH in the range of 1.3–1.5 V$_{RHE}$. γ-NiOOH with a layered double hydroxide structure is
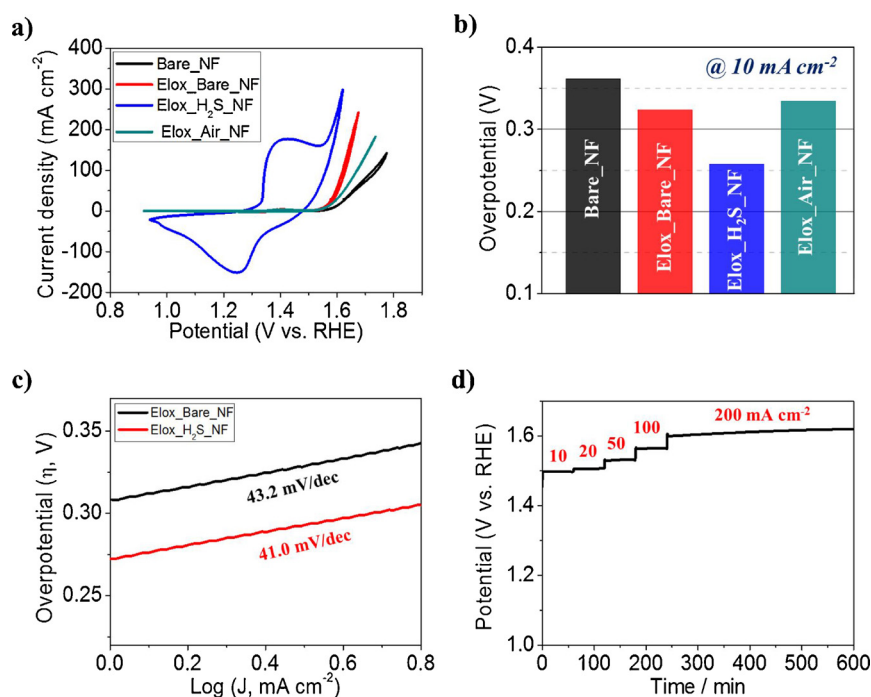
Fig. 4. (a) Cyclic voltammetry results of bare Ni foam (Bare_NF, black), electrochemically oxidized bare Ni foam (Elox_Bare_NF), electrochemically oxidized Ni-sulfide foam (Elox_H$_2$S_NF), and electrochemically oxidized Ni foam with air heat treatment (Elox_Air_NF). (b) Overpotentials of prepared samples at 10 mA cm^{-2}. (c) Tafel plots of electrochemically oxidized bare Ni foam (Elox_Bare_NF) and Ni-sulfide foam (Elox_H$_2$S_NF). (d) Electrocatalytic stability of electrochemically oxidized Ni-sulfide foam with stepwise current densities.

well known to have higher OER catalytic activity [11,43]. Based on these results, the active site of Elox_H$_2$S_NF for OER should be γ-NiOOH. The amount of γ-NiOOH also affected OER catalytic activity of sulfurized Ni electrocatalysts. To explain the improved catalytic activity of Elox_H$_2$S_NF from a different angle, XPS Fe 2p spectra were analyzed. Results are shown in Fig. S9 (Supporting Information).

It is known that Fe impurity from KOH electrolyte can be incorporated into γ-NiOOH structure and promote OER catalytic activity in Ni-based oxygen-evolution catalysts [55]. Bell et al. have demonstrated that Fe impurity incorporated into γ-NiOOH could significantly improve OER catalytic activity by increasing OH$^-$ affinity compared to Ni sites [64]. They also proposed that the position of the incorporated Fe impurity into γ-NiOOH might be an important factor for OER catalytic activity. According to their theoretical computational analysis, edge-positioned Fe (Fig. S10a, Supporting Information) would have more efficient active sites than bridge positioned Fe (Fig. S10b, Supporting Information) [64]. XPS Fe 2p spectra of Elox_H$_2$S_NF showed an Fe trace (+3), suggesting that Fe was incorporated into the γ-NiOOH phase, not a segregated phase [64]. In addition, the amorphous phase of Elox_H$_2$S_NF including its partially ordered structure (see dark contrast dots in Fig. 2f–g) provided large defect sites, resulting in improved OER catalytic activity [65]. These results support the notion that the amorphous phase of electrochemically oxidized Ni-sulfide can provide large edge sites, thus increasing the incorporation site of Fe impurities into the γ-NiOOH phase with high OER catalytic activity.

Tafel plots of Elox_Bare_NF and Elox_H$_2$S_NF are shown in Fig. 4c. Obtained Tafel slopes for Elox_Bare_NF and Elox_H$_2$S_NF were 43.2 and 41.0 mV dec^{-1}, respectively, close to their theoretical value of 40 mV dec^{-1} involving pre-equilibrium process consisting of a one-electron electrochemical step with a possible chemical step followed by a one-electron electrochemical rate determining step [66]. The electrocatalytic stability of Elox_H$_2$S_NF was also investigated using galvanostatic chronopotentiometric experiments with a gradual increase of current density up to 200 mA cm^{-2}. Results are shown in Fig. 4d. The electrochemically oxidized Ni-sulfide catalyst was found to be quite stable for 10 hours. H$_2$ and O$_2$ gas products under chronopotentiometric condition were further quantified and the ratio between H$_2$ and O$_2$ was also calculated. Results are shown in Fig. S11 (Supporting Information). The calculated value was 2 for 5 hours, demonstrating a high selectivity

toward water oxidation reaction.

Meanwhile, Ni-sulfide compounds have been regarded as promising materials for supercapacitor applications [67–72]. Our Elox_H$_2$S_NF also showed an electrochemical performance for capacitance measured in 1 M KOH. Details of supercapacitor properties of our samples were not described here to avoid confusion with our main subject (water oxidation). Instead, they were summarized in supporting information (Fig. S12, Supporting Information). Furthermore, sulfide derived sample was firstly introduced for OER in a CO$_2$-saturated bicarbonate (neutral) electrolyte system beyond alkaline media. This neutral environment is commonly found in CO$_2$ electro-reduction. Its better performance of Elox_H$_2$S_NF than the bare sample was briefly discussed in supporting information (Figs. S13–S15, Supporting Information).

4. Conclusions

A new preparation process of Ni-based electrocatalyst via thermal sulfurization followed by electrochemical oxidation conversion step was described in this study, resulting in significantly enhanced OER catalytic activity. During the electrochemical activation process, sulfur near the surface of Ni-sulfide (Ni$_3$S$_2$) formed by sulfurization was depleted and partially replaced by oxygen producing nano-sized particles with layered structure in amorphous matrix. Various spectroscopic analyses confirmed that sulfur in Ni-sulfide could act as an activator to create Ni(OH)$_2$/NiOOH mixtures on Ni-based electrocatalyst surface. Therefore, conversion of Ni$_3$S$_2$ top layer into mixed amorphous/crystalline Ni(OH)$_2$ and NiOOH might provide numerous active sites for water oxidation especially with Fe incorporation, thereby leading to great improvement in OER performance. Our study could offer an important insight into metal-chalcogenide electrocatalysts for water oxidation.

Appendix A. Supplementary data

Supplementary data, CV, LSV, GCD test data and SEM, TEM, XRD, XPS, Raman results, associated with this article can be found in the online version, at doi:https://doi.org/10.1016/j.apcatb.2018.03.083.

References

[1] J.A. Turner, Science 305 (2004) 972–974.
[2] H. Dau, C. Limberg, T. Reier, M. Risch, S. Roggan, P. Strasser, ChemCatChem 2 (2010) 724–761.
[3] N.B. Halck, V. Petrykin, P. Krtil, J. Rossmeisl, Phys. Chem. Chem. Phys. 16 (2014) 13682–13688.
[4] M. Gao, W. Sheng, Z. Zhuang, Q. Fang, S. Gu, J. Jiang, Y. Yan, J. Am. Chem. Soc. 136 (2014) 7077–7084.
[5] C.C.L. McCrory, S. Jung, I.M. Ferrer, S.M. Chatman, J.C. Peters, T.F. Jaramillo, J. Am. Chem. Soc. 137 (2015) 4347–4357.
[6] T. Reier, M. Oezaslan, P. Strasser, ACS Catal. 2 (2012) 1765–1772.
[7] H.-S. Oh, H.N. Nong, T. Reier, M. Gliech, P. Strasser, Chem. Sci. 6 (2015) 3321–3328.
[8] H.N. Nong, H.-S. Oh, T. Reier, E. Willinger, M.-G. Willinger, V. Petkov, D. Teschner, P. Strasser, Angew. Chem. Int. Ed. 54 (2015) 2975–2979.
[9] L.-A. Stern, X. Hu, Faraday Discuss. 176 (2014) 363–379.
[10] M.S. Burke, L.J. Enman, A.S. Batchellor, S. Zou, S.W. Boettcher, Chem. Mater. 27 (2015) 7549–7558.
[11] L. Trotochaud, S.L. Young, J.K. Ranney, S.W. Boettcher, J. Am. Chem. Soc. 136 (2014) 6744–6753.
[12] F. Dionigi, P. Strasser, J. Am. Chem. Soc. 6 (2016) 1600621.
[13] A. Bergmann, E. Martinez-Moreno, D. Teschner, P. Chernev, M. Gliech, J.F. de Araújo, T. Reier, H. Dau, P. Strasser, Nat. Commun. 6 (2015) 8625.
[14] J. Kim, X. Yin, K.-C. Tsao, S. Fang, H. Yang, J. Am. Chem. Soc. 136 (2014) 14646–14649.
[15] J. Suntivich, K.J. May, H.A. Gasteiger, J.B. Goodenough, Y. Shao-Horn, Science 334 (2011) 1383–1385.
[16] J.O.M. Bockris, T. Otagawa, J. Electrochem. Soc. 131 (1984) 290–302.
[17] W. Zhou, X.-J. Wu, X. Cao, X. Huang, C. Tan, J. Tian, H. Liu, J. Wang, H. Zhang, Energy Environ. Sci. 6 (2013) 2921–2924.
[18] M.-R. Gao, Y.-F. Xu, J. Jiang, Y.-R. Zheng, S.-H. Yu, J. Am. Chem. Soc. 134 (2012) 2930–2933.
[19] M.-R. Gao, Y.-F. Xu, J. Jiang, S.-H. Yu, Chem. Soc. Rev. 42 (2013) 2986–3017.
[20] K. Jin, J. Park, J. Lee, K.D. Yang, G.K. Pradhan, U. Sim, D. Jeong, H.L. Jang, S. Park, D. Kim, N.-E. Sung, S.H. Kim, S. Han, K.T. Nam, J. Am. Chem. Soc. 136 (2014) 7435–7443.
[21] A. Sartorel, M. Carraro, G. Scorrano, R.D. Zorzi, S. Geremia, N.D. McDaniel, S. Bernhard, M. Bonchio, J. Am. Chem. Soc. 130 (2008) 5006–5007.
[22] Q. Yin, J.M. Tan, C. Besson, Y.V. Geletii, D.G. Musaev, A.E. Kuznetsov, Z. Luo, K.I. Hardcastle, C.L. Hill, Science 328 (2010) 342–345.
[23] V. Artero, M. Chavarot-Kerlidou, M. Fontecave, Angew. Chem. Int. Ed. 50 (2011) 7238–7266.
[24] B. You, Y. Sun, Hierarchically porous nickel sulfide multifunctional superstructures, Adv. Energy Mater. 6 (2016) 1502333.
[25] A. Sivanantham, P. Ganesan, S. Shanmugam, Adv. Funct. Mater. 26 (2016) 4661–4672.
[26] G.-F. Chen, T.Y. Ma, Z.-Q. Liu, N. Li, Y.-Z. Su, K. Davey, S.-Z. Qiao, Adv. Funct. Mater. 26 (2016) 3314–3323.
[27] L.-L. Feng, G. Yu, Y. Wu, G.-D. Li, H. Li, Y. Sun, T. Asefa, W. Chen, X. Zou, J. Am. Chem. Soc. 137 (2015) 14023–14026.
[28] H. Li, Y. Shao, Y. Su, Y. Gao, X. Wang, Chem. Mater. 28 (2016) 1155–1164.
[29] O. Mabayoje, A. Shoola, B.R. Wygant, C.B. Mullins, ACS Energy Lett. 1 (2016) 195–201.
[30] H. Vandenborre, P. Vermeiren, R. Leysen, Electrochim. Acta 29 (1984) 297–301.
[31] X. Long, G. Li, Z. Wang, H. Zhu, T. Zhang, S. Xiao, W. Guo, S. Yang, J. Am. Chem. Soc. 137 (2015) 11900–11903.
[32] D.Y. Chung, J.W. Han, D.-H. Lim, J.-H. Jo, S.J. Yoo, H. Lee, Y.-E. Sung, Nanoscale 7 (2015) 5157–5163.
[33] X. Shang, X. Li, W.-H. Hu, B. Dong, Y.-R. Liu, G.-Q. Han, Y.-M. Chai, Y.-Q. Liu, C.-G. Liu, Appl. Surf. Sci. 378 (2016) 15–21.
[34] J.S. Kang, Y. Noh, J. Kim, H. Choi, T.H. Jeon, D. Ahn, J.-Y. Kim, S.-H. Yu, H. Park, J.-H. Yum, W. Choi, D.C. Dunand, H. Choe, Y.-E. Sung, Angew. Chem. Int. Ed. 56 (2017) 6583–6588.
[35] J.S. Kang, H. Choi, J. Kim, H. Park, J.-Y. Kim, J.-W. Choi, S.-H. Yu, K.J. Lee, Y.S. Kang, S.H. Park, Y.-H. Cho, J.-H. Yum, D.C. Dunand, H. Choe, Y.-E. Sung, Small 13 (2017) 1701458.
[36] S.M. El-Refaei, M.I. Awad, B.E. El-Anadouli, M.M. Saleh, Electrochim. Acta 92 (2013) 460–467.
[37] J.S. Chen, J. Ren, M. Shalom, T. Fellinger, M. Antonietti, ACS Appl. Mater. Interfaces 8 (2016) 5509–5516.
[38] M.B. Stevens, L.J. Enman, A.S. Batchellor, M.R. Cosby, A.E. Vise, C.D.M. Trang, S.W. Boettcher, Chem. Mater. 29 (2017) 120–140.
[39] B.M. Hunter, W. Hieringer, J.R. Winkler, H.B. Gray, A.M. Muller, Energy Environ. Sci. 9 (2016) 1734–1743.
[40] M. Bouroushian, Electrochemistry of Metal Chalcogenides, Springer Berlin Heidelberg, Berlin, Heidelberg, 2010, pp. 57–75.
[41] N. Cheng, Q. Liu, A.M. Asiri, W. Xing, X. Sun, J. Mater. Chem. A 3 (2015) 23207–23212.
[42] N. Jiang, Q. Tang, M. Sheng, B. You, D.-e. Jiang, Y. Sun, Catal. Sci. Technol. 6 (2016) 1077–1084.
[43] S. Klaus, Y. Cai, M.W. Louie, L. Trotochaud, A.T. Bell, J. Phys. Chem. C 119 (2015) 7243–7254.
[44] D. Singh, J. Electrochem. Soc. 145 (1998) 116–120.
[45] H. Zhang, X. Zhang, D. Zhang, X. Sun, H. Lin, C. Wang, Y. Ma, J. Phys. Chem. B 117 (2013) 1616–1627.
[46] U. Singh, A. Banerjee, D. Mhamane, A. Suryawanshi, K.K. Upadhyay, S. Ogale, RSC Adv. 4 (2014) 39875–39883.
[47] N. Parveen, M.H. Cho, Sci. Rep. 6 (2016) 27318.
[48] Y. Xia, W. Zhang, Z. Xiao, H. Huang, H. Zeng, X. Chen, F. Chen, Y. Gan, X. Tao, J. Mater. Chem. 22 (2012) 9209–9215.
[49] S.J. Kim, G.J. Park, B.C. Kim, J.K. Chung, G.G. Wallace, S.Y. Park, Synth. Met. 161 (2012) 2641–2646.
[50] Z. Cheng, H. Abernathy, M. Liu, J. Phys. Chem. C 111 (2007) 17997–18000.
[51] J.H. Wang, Z. Cheng, J.L. Brdas, M. Liu, J. Chem. Phys. 127 (2007).
[52] K.S. Joya, X. Sala, Phys. Chem. Chem. Phys. 17 (2015) 21094–21103.
[53] R. Kostecki, F. McLarnon, J. Electrochem. Soc. 144 (1997) 485–493.
[54] M.C. Biesinger, L.W.M. Lau, A.R. Gerson, R.S.C. Smart, Phys. Chem. Chem. Phys. 14 (2012) 2434–2442.
[55] M.C. Biesinger, B.P. Payne, A.P. Grosvenor, L.W.M. Lau, A.R. Gerson, R.S.C. Smart, Appl. Surf. Sci. 257 (2011) 2717–2730.
[56] J. Heo, J.S. Sanghera, J.D. Mackenzie, J. Non-Cryst. Solids 101 (1988) 23–30.
[57] A.N. Buckley, R. Woods, J. Appl. Electrochem. 21 (1991) 575–582.
[58] L. Trotochaud, J.K. Ranney, K.N. Williams, S.W. Boettcher, J. Am. Chem. Soc. 134 (2012) 17253–17261.
[59] C. Xiao, Y. Li, X. Lu, C. Zhao, Adv. Funct. Mater. 26 (2016) 3515–3523.
[60] M.W. Louie, A.T. Bell, J. Am. Chem. Soc. 135 (2013) 12329–12337.
[61] B.J. Trześniewski, O. Diaz-Morales, D.A. Vermaas, A. Longo, W. Bras, M.T.M. Koper, W.A. Smith, J. Am. Chem. Soc. 137 (2015) 15112–15121.
[62] D. Giovanelli, N.S. Lawrence, L. Jiang, T.G.J. Jones, R.G. Compton, Sens. Actuators B 88 (2003) 320–328.
[63] D. Giovanelli, N.S. Lawrence, S.J. Wilkins, L. Jiang, T.G.J. Jones, R.G. Compton, Talanta 61 (2003) 211–220.
[64] D. Friebel, M.W. Louie, M. Bajdich, K.E. Sanwald, Y. Cai, A.M. Wise, M.-J. Cheng, D. Sokaras, T.-C. Weng, R. Alonso-Mori, R.C. Davis, J.R. Bargar, J.K. Nørskov, A. Nilsson, A.T. Bell, J. Am. Chem. Soc. 137 (2015) 1305–1313.
[65] Y. Yang, H. Fei, G. Ruan, C. Xiang, J.M. Tour, ACS Nano 8 (2014) 9518–9523.
[66] E.B. Castro, C.A. Gervasi, Int. J. Hydrogen Energy 25 (2000) 1163–1170.
[67] S.W. Chou, J.Y. Lin, J. Electrochem. Soc. 160 (2013).
[68] Z. Dai, X. Zang, J. Yang, C. Sun, W. Si, W. Huang, X. Dong, ACS Appl. Mater. Interfaces 7 (2015) 25396–25401.
[69] C. Sun, M. Ma, J. Yang, Y. Zhang, P. Chen, W. Huang, X. Dong, Sci. Rep. 4 (2014) 7054.
[70] H. Pang, C. Wei, X. Li, G. Li, Y. Ma, S. Li, J. Chen, J. Zhang, Sci. Rep. 4 (2014) 3577.
[71] W. Wei, L. Mi, Y. Gao, Z. Zheng, W. Chen, X. Guan, Chem. Mater. 26 (2014) 3418–3426.
[72] A. Wang, H. Wang, S. Zhang, C. Mao, J. Song, H. Niu, B. Jin, Y. Tian, Appl. Surf. Sci. 282 (2013) 704–708.